Direct Imaging Au Nanoparticle Migration Inside Mesoporous Silica Channels

Zhengwang Liu,[†] Renchao Che,[*,†] Ahmed A. Elzatahry,[‡,||] and Dongyuan Zhao[*,†]

[†]Department of Chemistry and Shanghai Key Lab of Molecular Catalysis and Innovative Materials, State Key Laboratory of Molecular Engineering of Polymers and Advanced Materials Laboratory, Fudan University, Shanghai 200433, P.R. China, [‡]Department of Chemistry, College of Science, King Saud University, Riyadh 11451, Saudi Arabia, and [||]Polymer Materials Research Department, Advanced Technology and New Materials Research Institute, City of Scientific Research and Technology Applications, New Borg El-Arab City, Alexandria 21934, Egypt

ABSTRACT Supported metal nanoparticle (NP) catalysts have been widely used in many industry processes and catalytic reactions. Catalyst deactivation is mainly caused by the sintering of supported metal NPs. Hence, understanding the metal NPs' sintering behaviors has great significance in preventing catalyst deactivation. Here we report the metal particle migration inside/between mesochannels by
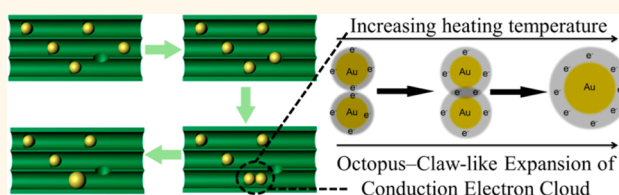
scanning transmission electron microscopy and electron energy loss spectroscopy *via* an *in situ* TEM heating technique. A sintering process is proposed that particle migration predominates, driven by the difference of gravitational potential from the height of the uneven internal surface of the mesopores; when the distance of the gold nanoparticles with a size of about 3 and 5 nm becomes short after migration, the coalescence process is completed, which is driven by an "octopus-claw-like" expansion of a conduction electron cloud outside the Au NPs. The supports containing an abundance of micropores help to suppress particle migration and coalescence. Our findings provide the understanding toward the rational design of supported industrial catalysts and other nanocomposites with enhanced activity and stability for applications such as batteries, catalysis, drug delivery, gas sensors, and solar cells.

KEYWORDS: particle migration · *in situ* TEM · gold nanoparticles · mesoporous materials

Supported metal nanoparticle (NP) catalysts have been widely used in industrial processes, including methane steam reforming, catalytic hydrogenation and dehydrogenation, and oxygen reduction.[1−4] Catalytic performance and stability of these supported metal NP catalysts depended significantly on one of the key factors: size of metal NPs;[5−14] however, the sintering behaviors caused by elevated temperature are a predominant cause of deactivation for metal NPs in industrial catalysts. In particular, rigorous environment such as high reaction temperature and reactive gas during the catalysis process often expedites the sintering. Consequently, in order to gain a better understanding of the sintering mechanism of metal NPs, *in situ* monitoring of the sintering process of the supported metal NP catalysts has been attracting more interest. Recently, Simonsen *et al.*[15,16] have put forward Ostwald ripening of Pt NPs on the planar Al_2O_3 and SiO_2 supports under exposure to 10 mbar air at 650 °C by *in situ* TEM experiments.

Yoshida *et al.*[17,18] also observed the Ostwald ripening of Pt NPs on amorphous carbon supports by using high-energy irradiation (300 keV). So the sintering behaviors of supported metal NPs are typically ascribed to mass-transport mechanisms containing particle or atomic migration.[19,20] The particle migration process describes the mobility of particles in a Brownian-like motion on supports, followed by the coalescence growth. The atomic migration mechanism refers to the Ostwald ripening process in which sintering occurs by the diffusion of atoms or atomic species either on the surface of the supports or through the gas phase between immobile NPs. Due to ordered and controllable mesopores, mesoporous silica is a kind of efficient catalyst support for metal NPs, in particular, providing an excellent model with spatial confinement to the study of the metal NP agglomeration.[21−28] However, the understanding about the sintering process of metal NPs confined in the mesochannels of mesoporous materials is still unclear.
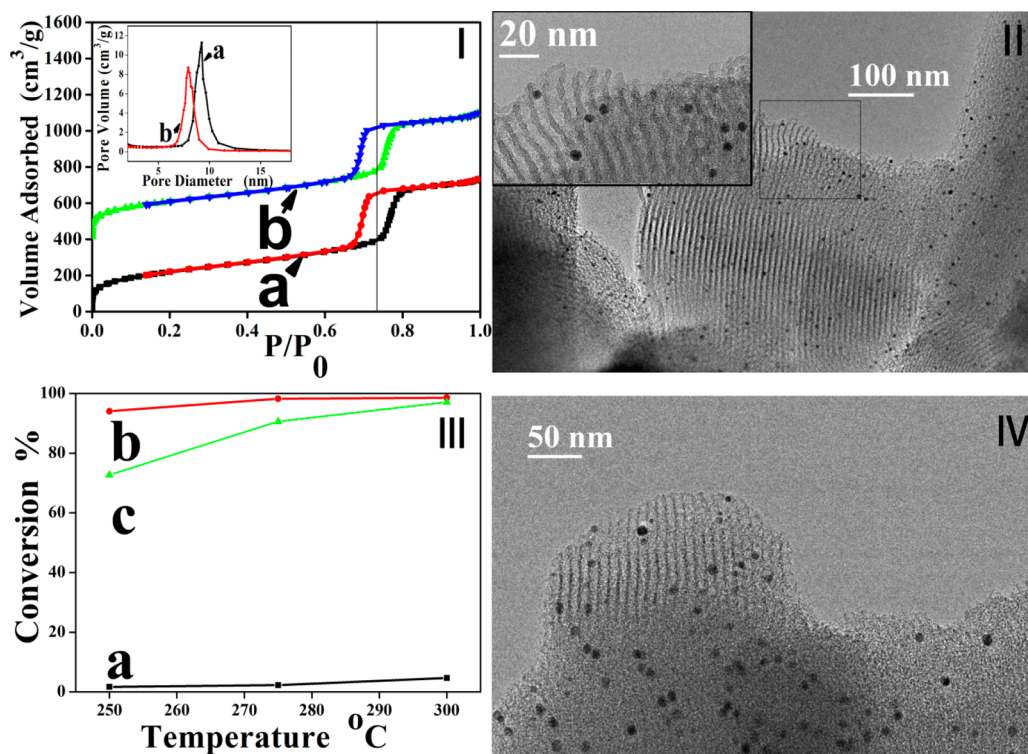
©2014 American Chemical Society

Figure 1. (I) N_2 adsorption−desorption isotherms of (a) SBA-15-100 sample and (b) Au-SBA-15-100-300 sample (in order to be observed clearly, the ordinate of adsorption−desorption isotherms of sample b increased by +400) and (inset) pore size distribution curves calculated from the absorption branch of samples a and b by the BJH method. (II) Low-magnification and high-magnification (inset) TEM images of sample b. (III) Conversions of benzyl alcohol under gas phase oxidation over sample a (SBA-15−100), sample b (Au-SBA-15-100-300) after calcination at 300 °C, and sample c (Au-SBA-15-100-500) after calcination at 500 °C. (IV) TEM image of sample c.

Herein, taking Au-SBA-15 for an example, we report the migration of metal Au NPs inside the ordered mesopore channels *via* combined *in situ* heating TEM observations including scanning transmission electron microscopy (STEM) and electron energy loss spectroscopy (EELS) up to 700 °C. It is the first time the migration of Au NPs along a mesochannel and even migration from a mesochannel to neighboring one is observed. A particle migration mechanism is proposed where particle migration is driven by the difference of gravitational potential from the height of the uneven internal surface of the mesopores; subsequently, when interparticle distance becomes short, a conduction electron cloud outside the metal NPs can expand similarly to the stretching of an "octopus-claw", and eventually metal NPs merge with each other.

RESULTS AND DISCUSSION

Three ordered mesoporous silica SBA-15 with different pore diameters were synthesized *via* changing the hydrothermal treatment temperature from 60 to 100 to 130 °C and chosen as the supports. The explanation for the names of samples, Au-SBA-15-T_1-T_2, is listed, the mass ratio of Au to SiO_2 in all samples: 0.5 wt %; T_1: hydrothermal temperature of SBA-15; T_2: pretreatment temperature of as-made Au-SBA-15. SAXS patterns (Figure S1 in Supporting Information) and N_2 adsorption/desorption isotherms (Figure S2 in Supporting Information) demonstrate that all three samples have highly ordered mesostructure with two-dimensional (2-D) hexagonal (*p6mm*) symmetry. The Barrett−Joyner−Halenda (BJH) pore size distribution curves (Figure S3 in Supporting Information) show that the pore diameters of SBA-15-60, SBA-15-100, and SBA-15-130 are 5.8, 9.2, and 11.8 nm, respectively. The micropore volumes inside the mesopore walls of the three supports (Table S1) are calculated to be ∼0.01 cm^3/g (SBA-15-60), 0.09 cm^3/g (SBA-15-100). and 0.04 cm^3/g (SBA-15-130), confirming the existence of an uneven internal surface of the mesochannels. As for the SBA-15-130 sample, the micropore volume decreases after high hydrothermal temperature treatment (at 130 °C) because the micropores inside the silica pore walls become the mesotunnels connecting the neighboring mesopores. To confirm whether the Au NPs were successfully confined inside the channels of mesoporous silica SBA-15, N_2 adsorption/desorption isotherms and TEM analysis were carried out after the metal Au NPs with a size of ∼3 nm were loaded into the SBA-15 supports. The N_2 adsorption/desorption isotherms (Figure 1I) exhibit a type IV curve with an H1 hysteresis loop, indicating that the structure of the Au-SBA-15-100-300 sample is similar to that of the same sample without loading Au NPs. Moreover, both

SAXS patterns of the two samples before and after loading Au NPs show similar features (Figure S4 in Supporting Information), revealing that the loading process does not affect the mesoporous structures. However, due to the Au NP loading, the average mesopore size and pore volume decrease from 9.23 to 8.75 nm and 1.13 to 1.08 cm^3/g, respectively (Table S1). TEM images of the Au-SBA-15-100-300 sample after a high-temperature calcination at 300 °C (Figure 1II) further demonstrate that Au NPs with a diameter of about 3−5 nm are successfully loaded into the mesopore of the SBA-15-100 support. The TEM images of the Au-SBA-15-100-500 sample after a high-temperature calcination at 500 °C (Figure 1IV) show that the size of Au NPs in the mesopore channels increase to reach about 6−10 nm in diameter, suggesting that a sintering process occurs. Toward the catalytic oxidation of benzyl alcohol (Figures 1III and S5), the catalytic performance of the Au-SBA-15-100-300 catalyst is higher than that of the Au-SBA-15-100-500 sample, indicating the degradation of catalytic performance due to the Au NP sintering caused by elevated temperature.

Scanning transmission electron microscopy high-angular annular dark-field (STEM-HAADF) images of the Au-SBA-15-100-300 sample before the heating treatments are shown in Figure 2a,b. Due to the largest atomic number (Z) of gold, its NPs normally show the brightest dots in the STEM-HAADF images. However, the framework of SiO_2 shows the weak stripey structure in the images. It was found that most of the Au NPs were homogeneously dispersed inside the mesochannels with a size mainly ranging from 3 to 5 nm (Figures 2a-0 h and S7). In all *in situ* heating experiments, the same Z height of each observed particle was guaranteed through fine adjustment, and the detailed procedures were described in the Supporting Information. Meanwhile, target temperature was obtained within about 15 min. When the temperature increased to 550 °C and was maintained for 1 h, both mesochannels and micropores inside the pore walls started to shrink and the pore size became smaller due to the dehydration−condensation of silanol groups (Figure 2a-1 h).

Unexpectedly, when the temperature was maintained at 550 °C for several more hours (3−9 h), one individual Au NP began to slowly migrate from one channel to its neighboring one through the mesotunnels[29] between the mesopores of the mesoporous silica SBA-15 supports (Figure 2a). Control experiments before/after heating (Figures S8 and S9) were performed, keeping the electron beam scanning for 10 min. It was obvious that no particle migration and coalescence were observed and particle size was kept constant, demonstrating that the electron beam did not drive the particle migration and coalescence as reported in the literature.[30] Meanwhile, to reduce the
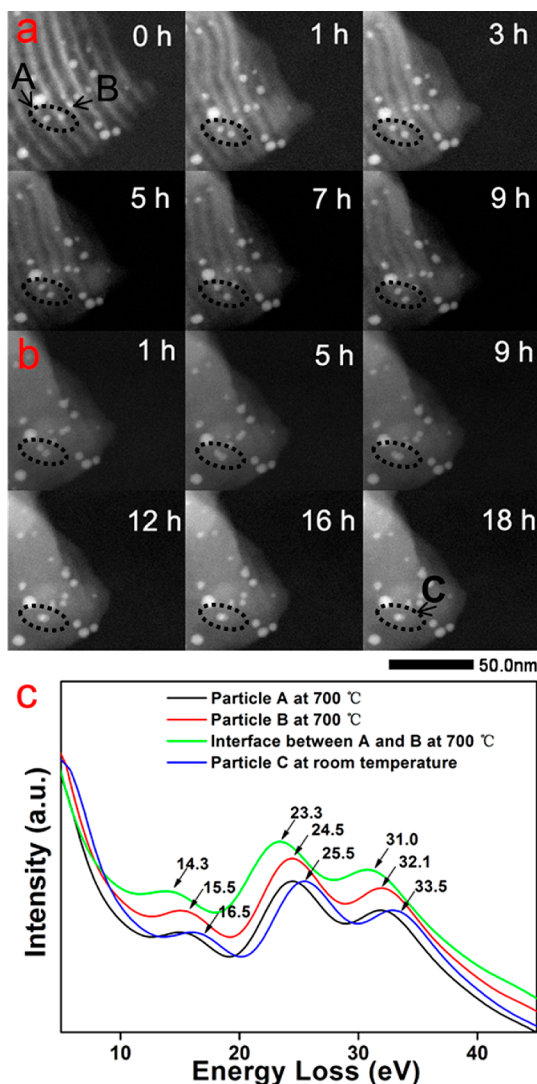

Figure 2. (a,b) STEM-HAADF images of the Au-SBA-15-100-300 sample under *in situ* TEM heating experiment at different heating temperatures: (a) 550 °C and (b) 700 °C. (c) Microarea EELS for particle A and particle B in panel a under *in situ* TEM heating experiment at 700 °C, showing the particle migration and the evolution of the conduction electron cloud outside the Au nanoparticles under *in situ* TEM heating conditions; when the distance of two particles becomes close enough (≤1 nm) (b-1 h), the original two individual particles are completely coalesced within 8 h (b-9 h).

electron beam as much as possible, the sample was exposed to the electron beam only when acquiring the images. Therefore, the particle migration should be driven by the uneven internal surface of the mesochannels. Eventually, the Au NP migrated and collided with a neighboring NP, followed by coalescence into a bigger one (Figure 2a,b). Compared with the particle size distribution in Figure S7, the particle size distribution in Figure S10 shows that the particles with 4.0 nm diameters are the maximum in all particles due to particle migration and coalescence.

While the sample was heated to 700 °C, high spatial resolution EELS analyses were performed only within
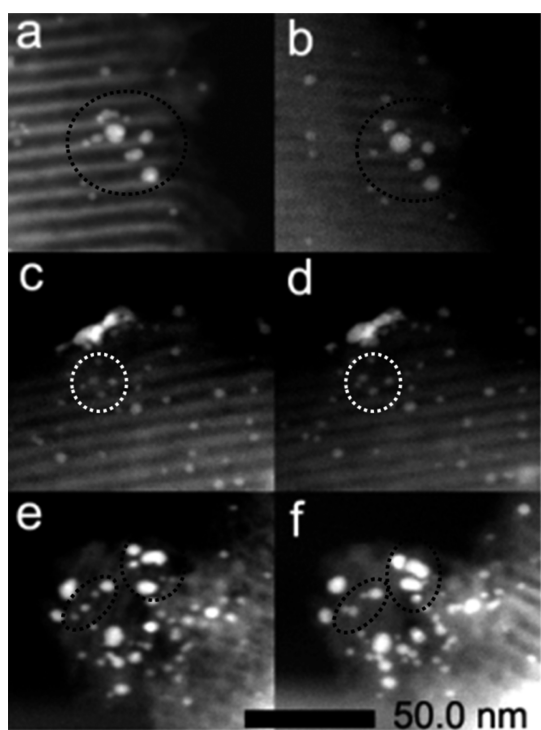
Figure 3. STEM-HAADF images of the Au-SBA-15-100-300 sample after calcination at 300 °C under *in situ* TEM heating experiment at different heating temperatures: (a) 0 h, (b) 1 h at 550 °C; (c) 0 h, (d) 1 h at 550 °C; (e) 0 h, (f) 1 h at 700 °C, showing particle migration under *in situ* TEM heating conditions.

particle A, particle B, and the interface between particles A and B (Figure 2c). The area covered by the electron beam could be well-controlled smaller than 0.3 nm size, thus guaranteeing enough spatial resolution. Three peaks located at ∼15.5, 24.5, and 32.1 eV of the EELS excitation energy were observed, which could be assigned to the plasmon peaks and intraband electron transitions of Au.[31]

Similar experimental phenomena were observed under different annealing conditions. When directly heated to 550 and 700 °C, the particles' migration along the mesochannels and coalescence was simultaneously observed (Figure 3). In addition, Ostwald ripening took place in a few regions when the particle size distribution was uneven (Figure S11).

The influence of the substrate morphology might play key roles in the sintering behavior of the supported metal NPs. Herein, the same amount of Au nanoparticles was loaded into the three different mesoporous silica SBA-15 with various pore sizes (Table S1). Careful STEM-HAADF images (Figure S12a–c) show that Au NPs were homogeneously dispersed inside the mesopore channels. The main size distributions of the Au-SBA-15-60-300, Au-SBA-15-100-300, and Au-SBA-15-130-300 samples were 6, 3, and 11 nm (Figures S13, S14, and S15), respectively. Evidently, the SBA-15-60 (mesopore diameter = 5.8 nm) and SBA-15-130 (mesopore diameter = 11.8 nm) supports facilitate the sintering of gold NPs inside the mesopores. However,

the SBA-15-100 (mesopore diameter = 9.2 nm) support hinders the sintering of Au NPs. There is no linear relationship between the sintering of gold NPs and mesopore diameter. According to the literature,[32] gold particles enter pores, embed into pore walls, and drill through the pore walls, which may offer more active sites for the catalytic reaction. As for the three supports, the micropores inside the mesopore walls provide the gold NPs with stable locations, which suppress the gold NP migration and coalescence. Because SBA-15-100 has the largest micropore volume among all the three supports (Table S1), it substantially suppresses the sintering behavior of Au NPs inside mesopores.

It is well-established that the incident electron energy can be lost during the inelastic scattering process of electron beam propagation through the metal NPs, and the energy loss caused by the conduction electron cloud is related to the ionization state and chemical activity of metal nanoparticles. The plasmon peaks result from the collective excitation energy of all the conduction electrons of the metal NPs. The energy loss by the electron beam is given by a simple expression: $E_p = \hbar(ne^2/\varepsilon_0 m)^{1/2}$, from which E_p is directly proportional to n, the conduction electron density of metal NPs. The positions of the three plasmon peaks of the interface between particles A and B (arrows in Figure 2a) shifted to a low-loss energy direction relative to a single one, suggesting the expansion of the conduction electron cloud of Au NPs (*i.e.*, n value decreased, green curve in Figure 2c). According to the literature,[30] to acquire the EELS, the particles and the space between the two particles must be exposed to a high-intensity electron beam for a prolonged period. This process alone could drive the particle coalescence. However, our control experiment (Figure S16) shows that a high-intensity electron beam does not drive the particle migration and coalesce without heating. When two spherical particles become sufficiently close, their surface plasmons can couple and exhibit a collective resonance, resulting in a lower energy longitudinal plasmon resonance.[33,34] The EELS experiment reported in the literature[33] showed that beam position could influence the intensity of the coupling of the surface plasmon, and no coupling of the surface plasmon was observed at the interparticle gap and the center of each particle. To exclude the coupling of the surface plasmon by beam position, the electron probe was placed at the center of a single particle A or B and the interface center between the two particles in the STEM-EELS mode. As such, the coupling of the surface plasmon can be minimized. Similar to the coupling of the surface plasmon, that of the bulk plasmon can also be minimized. EELS spectra (Figure S17) acquired from many Au NPs under *in situ* TEM heating conditions show that all the excitation energy values of the three peaks move to the low-energy direction under elevated temperature, also
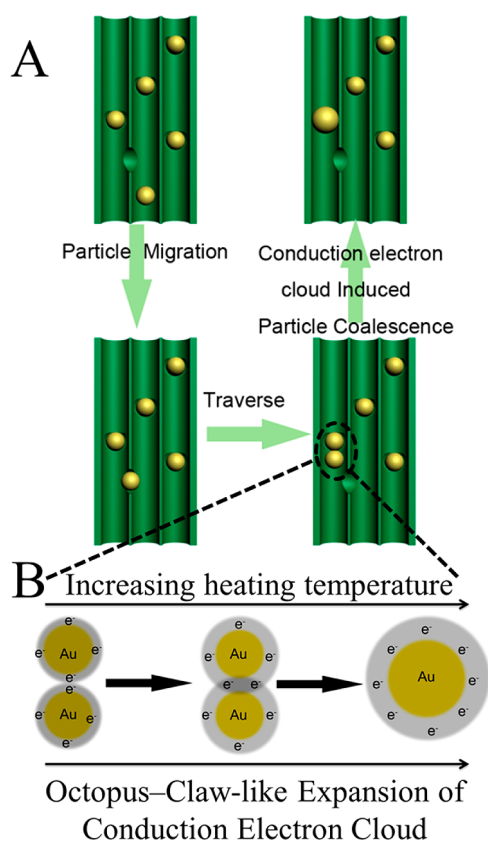
Scheme 1. Particle migration model: (A) particle migration and coalescence mechanism of Au nanoparticles in the mesopore channels of ordered mesoporous silica SBA-15; (B) particle coalescence induced by octopus-claw-like expansion of the conduction electron cloud.

confirming that high temperature can cause a lower energy plasmon resonance (*i.e.*, the expansion of conduction electron cloud outside the Au NPs). Therefore, induced by the expansion of the conduction electron cloud as a result of high temperature instead of the coupling effect of plasmon, suggesting that there could be electron tunneling[30] between particles prior to coalescence, the Au NP A can coalesce with its neighboring one B, forming a bigger particle C (arrows in Figure 2b).

CONCLUSIONS

In summary, we put forward a particle migration mechanism that is driven by the difference of gravitational potential from the height of the uneven internal surface of the mesopores. Moreover, when the distance of two particles becomes close enough (≤ 1 nm), particle coalescence induced by "octopus-claw-like" expansion of the conduction electron cloud is completed within 8 h (Scheme 1A,B). The morphology inside the mesochannels of the ordered mesoporous silica SBA-15 plays an important role in the sintering behavior of Au NPs. To suppress the agglomeration of metal particles, two key factors should be highlighted: (1) uniform size distribution of metal NPs; (2) supports

containing an abundance of micropores. Although the gas environment in industrial catalytic reactors also plays a role in the sintering, our work offers new insight into the sintering mechanism of supported metal NPs, more importantly, in turn toward the rational design of nanocomposite catalysts with longer cycle life.

Conflict of Interest: The authors declare no competing financial interest.

REFERENCES AND NOTES

1. Chen, Z.; Waje, M.; Li, W.; Yan, Y. Supportless Pt and PtPd Nanotubes as Electrocatalysts for Oxygen-Reduction Reactions. *Angew. Chem., Int. Ed.* **2007**, *46*, 4060–4063.
2. Liu, Z.-P.; Wang, C.-M.; Fan, K.-N. Single Gold Atoms in Heterogeneous Catalysis: Selective 1,3-Butadiene Hydrogenation over Au/ZrO$_2$. *Angew. Chem., Int. Ed.* **2006**, *45*, 6865–6868.
3. Ojeda, M.; Iglesia, E. Formic Acid Dehydrogenation on Au-Based Catalysts at Near-Ambient Temperatures. *Angew. Chem., Int. Ed.* **2009**, *48*, 4800–4803.
4. Challa, S. R.; Delariva, A. T.; Hansen, T. W.; Helveg, S.; Sehested, J.; Hansen, P. L.; Garzon, F.; Datye, A. K. Relating Rates of Catalyst Sintering to the Disappearance of Individual Nanoparticles during Ostwald Ripening. *J. Am. Chem. Soc.* **2011**, *133*, 20672–20675.
5. Turner, M.; Golovko, V. B.; Vaughan, O. P. H.; Abdulkin, P.; Berenguer-Murcia, A.; Tikhov, M. S.; Johnson, B. F. G.; Lambert, R. M. Selective Oxidation with Dioxygen by Gold Nanoparticle Catalysts Derived from 55-Atom Clusters. *Nature* **2008**, *454*, 981–983.
6. Liu, Y.; Jia, C. J.; Yamasaki, J.; Terasaki, O.; Schuth, F. Highly Active Iron Oxide Supported Gold Catalysts for CO Oxidation: How Small Must the Gold Nanoparticles Be? *Angew. Chem., Int. Ed.* **2010**, *49*, 5771–5775.
7. Herzing, A. A.; Kiely, C. J.; Carley, A. F.; Landon, P.; Hutchings, G. J. Identification of Active Gold Nanoclusters on Iron Oxide Supports for CO Oxidation. *Science* **2008**, *321*, 1331–1335.
8. Chen, M. S.; Goodman, D. W. The Structure of Catalytically Active Gold on Titania. *Science* **2004**, *306*, 252–255.
9. Liu, L.; Samjeske, G.; Nagamatsu, S.-i.; Sekizawa, O.; Nagasawa, K.; Takao, S.; Imaizumi, Y.; Yamamoto, T.; Uruga, T.; Iwasawa, Y. Dependences of the Oxygen Reduction Reaction Activity of Pd–Co/C and Pd–Ni/C Alloy Electrocatalysts on the Nanoparticle Size and Lattice Constant. *Top. Catal.* **2014**, *57*, 595–606.
10. Zhu, Y. J.; Zaera, F. Selectivity in the Catalytic Hydrogenation of Cinnamaldehyde Promoted by Pt/SiO$_2$ as a Function of Metal Nanoparticle Size. *Catal. Sci. Technol.* **2014**, *4*, 955–962.
11. Baldyga, L. M.; Blavo, S. O.; Kuo, C. H.; Tsung, C. K.; Kuhn, J. N. Size-Dependent Sulfur Poisoning of Silica-Supported Monodisperse Pt Nanoparticle Hydrogenation Catalysts. *ACS Catal.* **2012**, *2*, 2626–2629.
12. Li, G.; Tang, Z. Noble Metal Nanoparticle@Metal Oxide Core/Yolk-Shell Nanostructures as Catalysts: Recent Progress and Perspective. *Nanoscale* **2014**, *6*, 3995–4011.

13. Wilson, O. M.; Knecht, M. R.; Garcia-Martinez, J. C.; Crooks, R. M. Effect of Pd Nanoparticle Size on the Catalytic Hydrogenation of Allyl Alcohol. *J. Am. Chem. Soc.* **2006**, *128*, 4510–4511.

14. Johnson, J. A.; Makis, J. J.; Marvin, K. A.; Rodenbusch, S. E.; Stevenson, K. J. Size-Dependent Hydrogenation of *p*-Nitrophenol with Pd Nanoparticles Synthesized with Poly(amido)amine Dendrimer Templates. *J. Phys. Chem. C* **2013**, *117*, 22644–22651.

15. Simonsen, S. B.; Chorkendorff, I.; Dahl, S.; Skoglundh, M.; Sehested, J.; Helveg, S. Ostwald Ripening in a Pt/SiO$_2$ Model Catalyst Studied by *In-Situ* TEM. *J. Catal.* **2011**, *281*, 147–155.

16. Simonsen, S. B.; Chorkendorff, I.; Dahl, S.; Skoglundh, M.; Sehested, J.; Helveg, S. Direct Observations of Oxygen-Induced Platinum Nanoparticle Ripening Studied by *In-Situ* TEM. *J. Am. Chem. Soc.* **2010**, *132*, 7968–7975.

17. Yoshida, K.; Zhang, X. D.; Bright, A. N.; Saitoh, K.; Tanaka, N. Dynamic Environmental Transmission Electron Microscopy Observation of Platinum Electrode Catalyst Deactivation in a Proton-Exchange-Membrane Fuel Cell. *Nanotechnology* **2013**, *24*, 065705.

18. Yoshida, K.; Bright, A.; Tanaka, N. Direct Observation of the Initial Process of Ostwald Ripening Using Spherical Aberration-Corrected Transmission Electron Microscopy. *J. Electron. Microsc.* **2012**, *61*, 99–103.

19. Wynblatt, P.; Gjostein, N. A. Supported Metal Crystallites. *Prog. Solid State Chem.* **1975**, *9*, 21–58.

20. DeLaRiva, A. T.; Hansen, T. W.; Challa, S. R.; Datye, A. K. *In-Situ* Transmission Electron Microscopy of Catalyst Sintering. *J. Catal.* **2013**, *308*, 291–305.

21. Zhu, H. G.; Liang, C. D.; Yan, W. F.; Overbury, S. H.; Dai, S. Preparation of Highly Active Silica-Supported Au Catalysts for CO Oxidation by a Solution-Based Technique. *J. Phys. Chem. B* **2006**, *110*, 10842–10848.

22. Silva, R.; Biradar, A. V.; Fabris, L.; Asefa, T. Au/SBA-15-Based Robust and Convenient-To-Use Nanopowder Material for Surface-Enhanced Raman Spectroscopy. *J. Phys. Chem. C* **2011**, *115*, 22810–22817.

23. Chiang, C. W.; Wang, A. Q.; Wan, B. Z.; Mou, C. Y. High Catalytic Activity for CO Oxidation of Gold Nanoparticles Confined in Acidic Support Al-SBA-15 at Low Temperatures. *J. Phys. Chem. B* **2005**, *109*, 18042–18047.

24. Chen, L. F.; Hu, J. C.; Richards, R. Intercalation of Aggregation-Free and Well-Dispersed Gold Nanoparticles into the Walls of Mesoporous Silica as a Robust "Green" Catalyst for *n*-Alkane Oxidation. *J. Am. Chem. Soc.* **2009**, *131*, 914–915.

25. Eggenhuisen, T. M.; Friedrich, H.; Nudelman, F.; Zečević, J.; Sommerdijk, N. A. J. M.; de Jongh, P. E.; de Jong, K. P. Controlling the Distribution of Supported Nanoparticles by Aqueous Synthesis. *Chem. Mater.* **2013**, *25*, 890–896.

26. Yan, X.; Wang, X.; Tang, Y.; Ma, G.; Zou, S.; Li, R.; Peng, X.; Dai, S.; Fan, J. Ordered, Extra-large Mesopores with Highly Loaded Gold Nanoparticles: A New Sintering- and Coking-Resistant Catalyst System. *Chem. Commun.* **2013**, *49*, 7274–7276.

27. Prieto, G.; Zečević, J.; Friedrich, H.; de Jong, K. P.; de Jongh, P. E. Towards Stable Catalysts by Controlling Collective Properties of Supported Metal Nanoparticles. *Nat. Mater.* **2013**, *12*, 34–39.

28. Wang, S.; Zhao, Q.; Wei, H.; Wang, J.-Q.; Cho, M.; Cho, H. S.; Terasaki, O.; Wan, Y. Aggregation-Free Gold Nanoparticles in Ordered Mesoporous Carbons: Toward Highly Active and Stable Heterogeneous Catalysts. *J. Am. Chem. Soc.* **2013**, *135*, 11849–11860.

29. Fan, J.; Yu, C. Z.; Wang, L. M.; Tu, B.; Zhao, D. Y.; Sakamoto, Y.; Terasaki, O. Mesotunnels on the Silica Wall of Ordered SBA-15 To Generate Three-Dimensional Large-Pore Mesoporous Networks. *J. Am. Chem. Soc.* **2001**, *123*, 12113–12114.

30. Scholl, J. A.; García-Etxarri, A.; Koh, A. L.; Dionne, J. A. Observation of Quantum Tunneling between Two Plasmonic Nanoparticles. *Nano Lett.* **2013**, *13*, 564–569.

31. Reimer, L.; Zepke, U.; Moesch, J.; Schulze-Hillert, S. T.; Ross-Messemer, M.; Probst, W.; Weimer, E. *EELS Spectroscopy: A Reference Handbook of Standard Data for Identification and Interpretation of Electron Energy Loss Spectra and for Generation of Electron Spectroscopic Images*; Carl Zeiss, Electron Optics Division: Oberkochen, Germany, 1992.

32. Ma, C. Y.; Mu, Z.; Li, J. J.; Jin, Y. G.; Cheng, J.; Lu, G. Q.; Hao, Z. P.; Qiao, S. Z. Mesoporous Co$_3$O$_4$ and Au/Co$_3$O$_4$ Catalysts for Low-Temperature Oxidation of Trace Ethylene. *J. Am. Chem. Soc.* **2010**, *132*, 2608–2613.

33. Barrow, S. J.; Rossouw, D.; Funston, A. M.; Botton, G. A.; Mulvaney, P. Mapping Bright and Dark Modes in Gold Nanoparticle Chains Using Electron Energy Loss Spectroscopy. *Nano Lett.* **2014**, *14*, 3799–3808.

34. Kumar, J.; Wei, X.; Barrow, S.; Funston, A. M.; Thomas, K. G.; Mulvaney, P. Surface Plasmon Coupling in End-to-End Linked Gold Nanorod Dimers and Trimers. *Phys. Chem. Chem. Phys.* **2013**, *15*, 4258–4264.